Secondary Aneurysm Formation due to the Effects of a Primary Aneurysm

Bruno Beltran[1], Courtney Bruce[2], Daniel Burkow[3], Sarah Erickson[4], Ilyssa Summer[5], Sunmi Lee[5], Baojun Song[6]

July 31, 2012

[1] Department of Mathematics, Louisiana State University, Baton Rouge, Louisiana,
[2] Department of Biological Sciences, Arizona State University, Tempe, Arizona,
[3] Department of Applied Mathematics, Arizona State University, Glendale, Arizona,
[4] Department of Mathematics, Western Washington University, Bellingham, Washington,
[5] Department of AMLSS, Arizona State University, Tempe, Arizona
[6] Department of Mathematical Sciences, Montclair State University, Montclair, New Jersey

Abstract

Intracranial aneurysms are localized dilations of arterial vessels located around the Circle of Willis, an important network of arteries at the base of the brain. Aneurysms are at constant risk of hemorrhage; however, the number of benign cases carried by the populace, the dangers of treatment, and the risk of recurrence often null the efficacy of preventative surgery. Although the mechanisms behind the formation of individual intracranial aneurysms have been thoroughly modeled as the consequence of local hemodynamic conditions, previous simulations have concentrated on single aneurysms. Using OpenFOAM, an open source fluid dynamics toolkit, we model how changes in the hemodynamics within the Circle of Willis caused by the presence of a primary aneurysm can facilitate the formation of a secondary aneurysm. We determined the change in risk of developing a secondary aneurysm on the anterior communicating artery given a primary aneurysm at the bifurcation between the posterior communicator artery and the basilar artery. We found an average decrease in wall shear stress at the anterior communicating artery of 0-4%. Further, the necessary theory behind modeling turbulent flows with the Reynolds-Averaged Navier-Stokes equations is exposited.

1 Introduction

The presence of a single intracranial aneurysm is correlated with the appearance of multiple [11]. Single aneurysm growth has been extensively modeled and has been found to be largely attributed to low or oscillatory levels of wall shear stress (WSS) [3, 7, 9, 12, 13, 16, 19, 20]. Levels of WSS on an arterial wall are principally attributed to the hemodynamic conditions within the vessel [3, 7, 19, 20]. The lowest levels of WSS occur at arterial bifurcations [7]. Thus, in order to assess its impact on multiple aneurysm formation, we study the effects of a single aneurysm at an arterial bifurcation on the WSS at other bifurcations in the arterial structure.

Intracranial aneurysms are localized dilations of arteries in the brain and can be classified as saccular, fusiform, or dissecting [22]. Approximately 90% of intracranial aneurysms are saccular aneurysms, and they occur most frequently at arterial bifurcations of the Circle of Willis, a crucial cerebro-vascular structure [12], so we study saccular aneurysms exclusively.

Roughly 3.6-6% of the general population unknowingly has unruptured intracranial aneurysms [22], putting them at a continual risk of aneurysm rupture. This condition often results in a bleeding into the subarachnoid space, a subarachnoid hemorrhage. A subarachnoid hemorrhage has a mortality rate between 32% and 67% [8]. Saccular aneurysms are responsible for the most deaths due to hemorrhage [22], and the risk of hemorrhage increases further when multiple aneurysms are present [18]. Due to the risk of hemorrhage, many doctors choose to treat a patient with an unruptured aneurysm using either clipping or coiling methods. The clipping method involves placing a clip across the neck of the aneurysm, stopping the blood flow. On the other hand, coiling is the neuroendovascular approach which involves the usage of a microcatheter to coil a very thin platinum wire inside the aneurysm, sealing it, and reducing the pressure

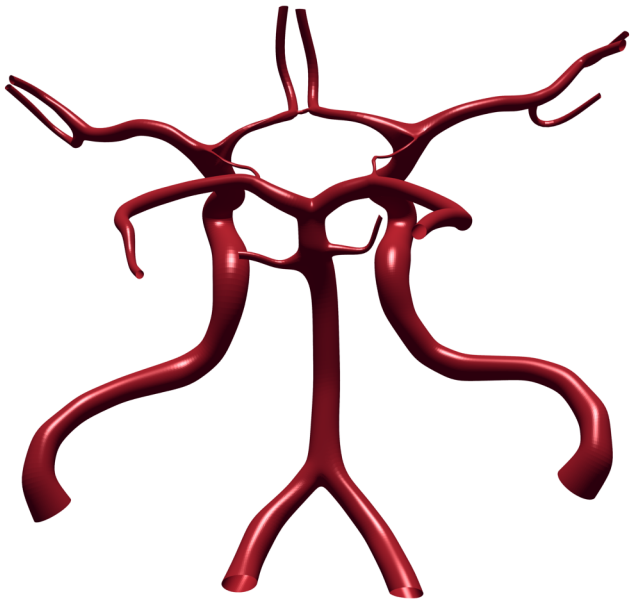

Figure 1: 3-D model of a large portion of the Circle of Willis constructed manually in Blender from healthy patient fMRI data. It was used as a template to construct the diseased vascular structures used in our simulations, as seen in Figure (5).

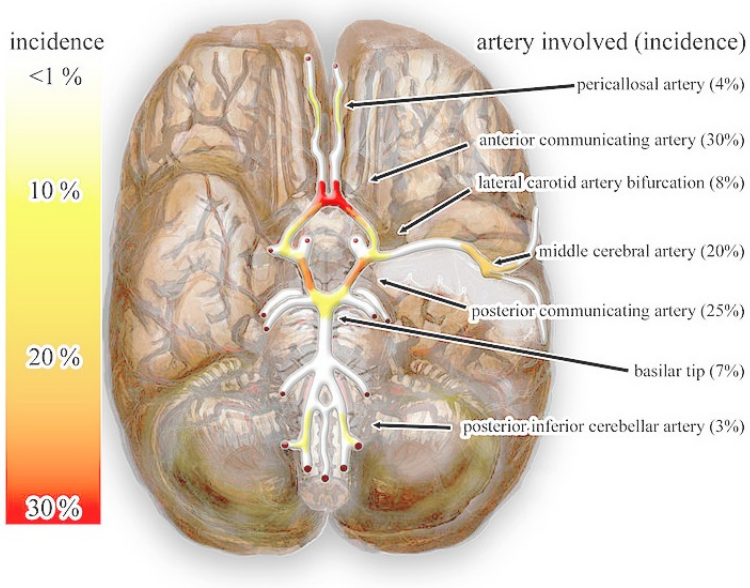

Figure 2: Common sites of saccular intracranial aneurysms [25]. We chose to place our aneurysms at the internal carotid artery bifurcations both because of the high incidence of aneurysms there and because of the high incidence downstream from there at the anterior communicating artery bifurcation.

Doctors could make more informed decisions concerning the treatment of patients with intracranial aneurysms if they could determine if a saccular aneurysm in the Circle of Willis is likely to cause more aneurysms further down the bloodstream, thus increasing the likelihood of a subarachnoid hemorrhage. Providing this insight is the primary motivation of this paper.

Aneurysms are caused by a myriad of factors, including genetic disorders and predispositions, hypertension, and collagen deficiency (such as that caused by arterial sclerosis) [22]. The factors we study in this paper are specifically the hemodynamics and wall biomechanics involved in the process of secondary aneurysm formation in the presence of a primary aneurysm. The deterioration of arterial walls is dependent on the WSS caused by blood flow within the artery, as WSS serves as both a mechanical instigator of aneurysm formation [21] and a bio-mechanical stimulus for the expression of genes critical to the health of arterial walls [23]. To study these stresses, we utilize a system of partial differential equations which can give us information about the velocity and pressure fields induced by the blood flow inside the Circle of Willis.

2 Model

In the following section, we briefly exposit modern theories for the modeling of turbulent fluid flows. Specifically, we will review the standard Navier-Stokes equations for incompressible fluid flow, the Reynolds-Averaged Navier-Stokes equations [14], and the Shear Stress Transport $k-\omega$ turbulence model [15].

2.1 Navier-Stokes Equations

We adopt the Navier-Stokes (NS) equations to model blood flow through the Circle of Willis because they can provide the velocity fields on which WSS directly depends [3, 7, 19, 20]. These equations model blood

as a continuum that completely fill the arteries, meaning that blood is considered infinitely divisible as opposed to an agglomerate of cells. Although blood is a non-Newtonian fluid [3], we adopt the simplifying assumption that it is. In other words, we assume that the stress versus strain rate curve is linear; that is, we assume the viscosity is only dependent on temperature and pressure, not on outside forces. Besides the conditions required by the NS equations, we assume that blood is incompressible, that it has constant density and viscosity, and that blood vessels are rigid. It has been shown that results obtained with these assumptions display the same qualitative dynamics as those obtained from less computationally efficient models that consider the compressibility of blood and the elasticity of vessel walls [1, 7].

The NS equations are formulated from Newton's Second Law of Motion, $\mathbf{F} = \frac{\mathrm{d}(\mathrm{m}\mathbf{U})}{\mathrm{dt}}$,where $\mathbf{F}$ is force, m is mass, and $\mathbf{U}$ is velocity, by using the laws of the conservation of mass and momentum. They can be expressed in terms of the velocity field, $\mathbf{U}(\mathbf{x}, t) \in \mathbb{R}^3$, and the pressure field, $p(\mathbf{x}, t)$, using Einstein summation convention as

$$\rho \frac{\partial U_i}{\partial x_i} = 0\,, \tag{2.1.1}$$

$$\rho \frac{\partial U_i}{\partial t} + \rho U_j \frac{\partial U_i}{\partial x_j} = \rho g_i - \frac{\partial p}{\partial x_i} + \mu \frac{\partial^2 U_j}{\partial x_j^2}\,, \tag{2.1.2}$$

where the indices $i, j \in \{1, 2, 3\}$ are used to indicate a component. In our model, the parameters g_i, ρ, and μ are constants representing the acceleration due to gravity, the density of the fluid, and its viscosity, respectively, as seen in Table 1.

Table 1: Navier-Stokes System Parameters [12]

Parameter	Description	Value	Units
$\mathbf{g} := (g_1, g_2, g_3)$	Acceleration Due To Gravity	$\|\|\mathbf{g}\|\| = 9.8$	$\frac{m}{s^2}$
μ	Viscosity	0.004	$\frac{kg}{m \cdot s}$
ρ	Blood Density	1050	$\frac{kg}{m^3}$

Alternatively, dividing through by ρ yields equivalent equations in terms of acceleration

$$\frac{\partial U_i}{\partial x_i} = 0\,, \tag{2.1.3}$$

$$\frac{\partial U_i}{\partial t} + U_j \frac{\partial U_i}{\partial x_j} = g_i - \frac{1}{\rho}\frac{\partial p}{\partial x_i} + \frac{\mu}{\rho}\frac{\partial^2 U_j}{\partial x_j^2}\,, \tag{2.1.4}$$

where

- $\frac{\partial U_i}{\partial t}$ corresponds to the local acceleration of the control volume.
- $U_j \frac{\partial U_i}{\partial x_j}$ is the convective acceleration.
- $\frac{1}{\rho}\frac{\partial p}{\partial x_i}$ is the pressure gradient.
- $\frac{\mu}{\rho}\frac{\partial^2 U_j}{\partial x_j^2}$ describes the surface stresses acting on the fluid.

The NS equations require boundary conditions, a 2-D manifold $\partial\Psi \subset \mathbb{R}^3$ enclosing the domain $\Psi \subset \mathbb{R}^3$, such that for some function F, $F(\mathbf{x}) = 0$ for all $\mathbf{x} \in \partial\Psi$. This condition restricts the domain of the solution to the 3-D space Ψ and is called a *no-slip* boundary condition. Finally, in order to specify a particular solution for the NS equations, we require initial values for the velocity and pressure fields $\mathbf{U}$ and p.

2.2 Reynolds-Averaged Navier-Stokes Equations

The principal turbulent shear stress on the artery walls is directly proportional to the turbulent kinetic energy in the wake region of the boundary layer [15], and can be calculated in this way by simulating the NS equations directly [10]. However, direct numerical simulation of turbulence through the NS equations is computationally expensive [10]. A more tractable approach is to use the Reynolds-Averaged Navier-Stokes (RANS) equations, which contain a tensor quantifying the turbulent stresses, the Reynolds stress tensor [14]. The RANS equations can be obtained by considering an unweighted (Reynolds) time average of the incompressible NS equations [14]. First, we take the Reynolds decomposition of the velocity and pressure,

$$U_i = \overline{U_i} + U_i' \,, \tag{2.2.1}$$

$$p = \overline{p} + p' \,. \tag{2.2.2}$$

Here $\overline{U_i}$ represents the time average of U_i, which is defined by

$$\overline{U_i}(\mathbf{x}) = \lim_{T\to\infty} \frac{1}{T} \int_{t_0}^{t_0+T} U_i \, dt \,.$$

Although it is common to derive the equations using this average, it is important to note that in the numerical calculations using the RANS equations, the Reynolds average, defined by

$$\overline{U_i}(\mathbf{x}, t) = \frac{1}{T(t)} \int_{t_0}^{t_0+T(t)} U_i \, dt \,,$$

for some T large enough to average out the turbulent fluctuations, is the defacto average of choice [14]. Specifically, this is the justification for assuming that $\overline{U_i}$ remains time dependent through the derivation even though in the true time average it is time independent. For a rigorous treatment of the relevant arguments see [14]. Finally, note that, in the Reynolds decomposition, U_i' represents the fluctuating portion of U_i about $\overline{U_i}$, thus $\overline{U_i'} = 0$ and $\overline{\overline{U_i}} = \overline{U_i}$.

Beginning with (2.1.1),

$$\rho \frac{\partial U_i}{\partial x_i} = 0 \,,$$

we make the substitutions indicated in (2.2.1),

$$\rho \frac{\partial}{\partial x_i} \left(\overline{U_i} + U_i' \right) = 0 \,,$$

and take the Reynolds average to get

$$\rho \frac{\partial}{\partial x_i} \left(\overline{\overline{U_i} + U_i'} \right) = 0 \,,$$

and

$$\rho \frac{\partial}{\partial x_i} \left(\overline{U_i} + \overline{U_i'} \right) = 0 \,.$$

However, since $\overline{U_i'} = 0$,

$$\rho \frac{\partial \overline{U_i}}{\partial x_i} = 0 \,. \tag{2.2.3}$$

Similarly, we divide (2.1.2) through by ρ and use the relationship $\nu = \mu/\rho$ to obtain

$$\frac{\partial U_i}{\partial t} + \frac{\partial}{\partial x_j} \left(U_i U_j \right) = g_i - \frac{1}{\rho} \frac{\partial p}{\partial x_i} + \nu \frac{\partial^2 U_j}{\partial x_j^2} \,,$$

where $\nu = 2.6 \times 10^{-6} \frac{m}{s^2}$ represents the kinematic viscosity. We then make the substitutions indicated in (2.2.1) and (2.2.2) and take the Reynolds average, which yields

$$\frac{\partial}{\partial t}\left(\overline{\overline{U_i} + U_i'}\right) + \frac{\partial}{\partial x_j}\left(\overline{\overline{U_i} + U_i'}\right)\left(\overline{\overline{U_j} + U_j'}\right) = g_i - \frac{1}{\rho}\frac{\partial}{\partial x_i}\left(\overline{\overline{p} + p'}\right) + \nu\frac{\partial^2}{\partial x_j^2}\left(\overline{\overline{U_j} + U_j'}\right) \ .$$

Recalling that $\overline{U_i'} = 0$ and expanding the factors on the left-hand side of the equation, we obtain

$$\frac{\partial \overline{U_i}}{\partial t} + \frac{\partial}{\partial x_j}\left[\overline{\overline{U_i}\,\overline{U_j}} + \overline{\overline{U_i}\,U_j'} + \overline{U_i'\overline{U_j}} + \overline{U_i U_j}\right] = g_i - \frac{1}{\rho}\frac{\partial \overline{p}}{\partial x_i} + \nu\frac{\partial^2 \overline{U_j}}{\partial x_j^2} \ ,$$

which further simplifies to

$$\frac{\partial \overline{U_i}}{\partial t} + \overline{U_j}\frac{\partial \overline{U_i}}{\partial x_j} = g_i - \frac{1}{\rho}\frac{\partial \overline{p}}{\partial x_i} + \nu\frac{\partial^2 \overline{U_j}}{\partial x_j^2} - \frac{\partial \overline{U_i' U_j'}}{\partial x_j} \ ,$$

and finally to

$$\frac{\partial \overline{U_i}}{\partial t} + \overline{U_j}\frac{\partial \overline{U_i}}{\partial x_j} = g_i + \frac{1}{\rho}\frac{\partial}{\partial x_j}\left(-\overline{p}\delta_{ij} + \mu\frac{\partial \overline{U_j}}{\partial x_j} - \rho\overline{U_i' U_j'}\right), \tag{2.2.4}$$

where δ_{ij} is the Kronecker delta defined such that $\delta_{ij} = 1$ if $i = j$, $\delta_{ij} = 0$ otherwise. While using the RANS equations decreases the computational complexity involved in calculating the turbulence, it introduces six new variables $\overline{U_i' U_j'}$ as the entries of the Reynolds stress tensor, yielding a system of equations that is no longer closed. To close the system of equations, we must include equations that give us more information about the turbulent kinetic energy in our model. A popular way to accomplish this is to use the Boussinesq approximation, which relates the Reynolds stress tensor and the mean velocity gradient in an equation of the form

$$-\overline{U_i' U_j'} = \nu_t \frac{\partial \overline{U_i}}{\partial x_j} \ . \tag{2.2.5}$$

The closing of the equations is then deferred to the modeling of ν_t, the kinematic eddy viscosity [10].

2.3 SST $k - \omega$ Equations

There exist several 'two-equation' turbulence transport models that can be used to evaluate ν_t when closing the RANS system by modeling the relationship between the Reynolds stress tensor and the mean velocity gradient as in (2.2.5). Of these turbulence transport models, the shear-stress transport (SST) $k-\omega$ model has been suggested as the most appropriate for hemodynamic simulations [2]. Here, k is the turbulent kinetic energy and ω is the dissipation of the kinetic energy throughout the fluid [15].

The SST $k - \omega$ model uses the 'standard' $k - \omega$ model for near-wall turbulence and the $k - \epsilon$ model for turbulence modeling away from the walls. The 'standard' $k - \omega$ model is given as

$$\frac{D\rho k}{Dt} = \tau_{ij}\frac{\partial \overline{U_i}}{\partial x_j} - \beta^*\rho\omega k + \frac{\partial}{\partial x_j}\left[\left(\mu + \sigma_{k_1}\mu_t\right)\frac{\partial k}{\partial x_j}\right] \tag{2.3.1}$$

$$\frac{D\rho\,\omega}{Dt} = \frac{\gamma_1}{\nu_t}\tau_{ij}\frac{\partial \overline{U_i}}{\partial x_j} - \beta_1\rho\omega^2 + \frac{\partial}{\partial x_j}\left[\left(\mu + \sigma_{\omega_1}\mu_t\right)\right] \ , \tag{2.3.2}$$

where $\frac{D}{Dt} = \frac{\partial}{\partial t} + \overline{U_i}\frac{\partial}{\partial x_i}$ is the material derivative. The tensor τ is the turbulent stress tensor, and the terms $\beta^*\rho\omega k$ and $\beta_1\rho\omega^2$ represent the destruction of k and ω, respectively [17]. The parameter $\mu_t = \rho\nu_t$ is the dynamic turbulent viscosity, and β^*, ω_{k_1}, γ_1, β_1, and σ_{ω_1} are proportionality constants. While this $k - \omega$ model is favored for its simplicity, numerical stability, and accuracy at predicting turbulent flow of fluid close to the wall of the vessel, it exaggerates the turbulence of the fluid as it moves away from the wall [15].

When the fluid moves farther away from the wall, the two-equation $k-\epsilon$ model,

$$\frac{Dk}{Dt} = \nu_t \left(\frac{\partial \overline{U_i}}{\partial x_j} + \frac{\partial \overline{U_j}}{\partial x_i} \right) \frac{\partial \overline{U_i}}{\partial x_j} - \epsilon + \frac{\partial}{\partial x_j} \left[\left(\nu + \frac{\nu_t}{\sigma_k} \right) \frac{\partial k}{\partial x_j} \right] , \tag{2.3.3}$$

$$\frac{D\epsilon}{Dt} = \frac{\epsilon}{k} c_{\epsilon 1} \nu_t \left(\frac{\partial \overline{U_i}}{\partial x_j} + \frac{\partial \overline{U_j}}{\partial x_i} \right) \frac{\partial \overline{U_i}}{\partial x_j} - c_{\epsilon 2} \frac{\epsilon^2}{k} + \frac{\partial}{\partial x_j} \left[\left(\nu + \frac{\nu_t}{\sigma_\epsilon} \right) \frac{\partial \epsilon}{\partial x_j} \right] , \tag{2.3.4}$$

more accurately predicts turbulent behavior. Here, k is again the turbulent kinetic energy and ϵ represents the dissipation rate thereof [17]. Making the substitution $\omega = \frac{\epsilon}{k\beta^*}$, we can formulate the $k-\epsilon$ model in terms of k and ω as

$$\frac{D\rho k}{Dt} = \tau_{ij} \frac{\partial \overline{U_i}}{\partial x_j} - \beta^* \rho \omega k + \frac{\partial}{\partial x_j} \left[(\mu + \sigma_{k_2} \mu_t) \frac{\partial k}{\partial x_j} \right] , \tag{2.3.5}$$

$$\frac{D\rho\omega}{Dt} = \frac{\gamma_2}{\nu_t} \tau_{ij} \frac{\partial \overline{U_i}}{\partial x_j} - \beta_2 \rho \omega^2 + \frac{\partial}{\partial x_j} \left[(\mu + \sigma_{\omega 2} \mu_t) \frac{\partial \omega}{\partial x_j} \right] + 2\rho\sigma_{\omega 2} \frac{1}{\omega} \frac{\partial k}{\partial x_j} \frac{\partial \omega}{\partial x_j} \tag{2.3.6}$$

[15]. The last term in (2.3.6)—which differentiates the $k-\epsilon$ and $k-\omega$ models—represents an added viscous diffusion term [4]. Since the $k-\epsilon$ model cannot be used to predict turbulence near a vessel wall—requiring a separate wall function to obtain correct near-wall results [5]—we must blend the two equations to accurately model turbulence.

Table 2: SST $k-\omega$ Model Functions [15]

Variable	Description	Value	Units
k	Turbulent Kinetic Energy (KE)	–	$\frac{m^2}{s^2}$
ω	Specific Dissipation of Turbulent KE	–	$\frac{1}{s}$
μ_t	Dynamic Turbulent Viscosity	$\rho\nu_t$	$\frac{kg}{ms}$
ν_t	Kinematic Turbulent Viscosity	$\frac{a_1 k}{\max\{a_1\omega, \Omega F_2\}}$	$\frac{m^2}{s}$

To combine the two different models according to the location where their results are most accurate, we multiply (2.3.1) and (2.3.2) by a blending function, F_1, defined in Table 3 and multiply (2.3.5) and (2.3.6) by $(1-F_1)$. Adding the corresponding equations together yields the SST $k-\omega$ model, first proposed in the American Institute of Aeronautics and Astronautics Journal by F. R. Menter and given as

$$\frac{D\rho k}{Dt} = \tau_{ij} \frac{\partial \overline{U_i}}{\partial x_j} - \beta^* \rho \omega k + \frac{\partial}{\partial x_j} \left[(\mu + \sigma_k \mu_t) \frac{\partial k}{\partial x_j} \right] ,$$

$$\frac{D\rho\omega}{Dt} = \frac{\gamma}{\nu_t} \tau_{ij} \frac{\partial \overline{U_i}}{\partial x_j} - \beta \rho \omega^2 + \frac{\partial}{\partial x_j} \left[(\mu + \sigma_\omega \mu_t) \frac{\partial \omega}{\partial x_j} \right] + 2(\rho - F_1)\rho\sigma_{\omega_2} \frac{1}{\omega} \frac{\partial k}{\partial x_j} \frac{\partial \omega}{\partial x_j} .$$

Finally, by solving the RANS equations in conjunction with the SST $k-\omega$ model, we can obtain velocity fields and pressures which account for changes in turbulent kinetic energy in the system. The kinematic eddy viscosity introduced in (2.2.5) can then be evaluated as

$$\nu_t = \frac{a_1 k}{\max\{a_1\omega, \Omega F_2\}} .$$

Table 3: SST $k-\omega$ Model Parameters [15]

Parameter			Description	Units
$\mathrm{CD}_{k\omega}$	=	$\max\left\{2\rho\sigma_{\omega_2}\frac{1}{\omega}\frac{\partial k}{\partial x_j}\frac{\partial \omega}{\partial x_j}, 10^{-20}\right\}$	Placeholder in $\arg_1$	*
$\arg_1$	=	$\min\left\{\frac{4\rho\sigma_{\omega_2}k}{\mathrm{CD}_{k\omega}y^2}; \max\left\{\frac{\sqrt{k}}{0.09\omega y}, \frac{500\nu}{y^2\omega}\right\}\right\}$	Placeholder in F_1	*
$\arg_2$	=	$\max\left\{2\frac{\sqrt{k}}{0.09\omega y}, \frac{500\nu}{y^2\omega}\right\}$	Placeholder in F_2	*
F_1	=	$\tanh\left(\arg_1^4\right)$	Blending Function	*
F_2	=	$\tanh\left(\arg_2^2\right)$	Parameter of ν_t	*
a_1	=	0.31	ν_t Constant	*
β^*	=	0.09	SST Model Constant	*
β	=	$0.0828 - 0.0078F_1$	Constant of Proportionality	*
γ	=	$0.440 - 0.113F_1$	Constant of Proportionality	*
σ_k	=	$1 - 0.15F_1$	Prandtl Number [4]	*
σ_ω	=	$0.856 - 0.356F_1$	Prandtl Number [4]	*
σ_{ω_2}	=	0.856	Prandtl Number [4]	*
S_{ij}	=	$\frac{1}{2}\left[\frac{\partial \overline{U_i}}{\partial x_j} + \frac{\partial \overline{U_j}}{\partial x_i}\right] - \frac{1}{3}\frac{\partial \overline{U_k}}{\partial x_k}\delta_{ij}$	Entries of Stress Tensor [6]	$\frac{1}{s}$
τ_{ij}	=	$2\mu_t\left(S_{ij} - \frac{1}{3}\frac{\partial \mu_k}{\partial x_k}\right) - \frac{2}{3}\rho k\delta_{ij}$	Entries of Turbulent Stress Tensor [17]	$\frac{kg}{m\cdot s^2}$
Ω	=	$\|\nabla \times \mathbf{U}\|$	Absolute Value of KE of Vorticity	$\frac{1}{s}$
y			Distance to Nearest Surface	m

* represents a unitless quantity

Since the RANS and SST $k-\omega$ equations do not have known analytical solutions, we utilize the software package OpenFOAM, inputting the values from Tables 2 and 3, to numerically approximate $\mathbf{U}$ and p, exactly the fields we need.

2.4 Summary of Model

To study the velocity and pressure inside the Circle of Willis while including the effects of turbulence, we use the RANS equations.

$$\rho\frac{\partial \overline{U_i}}{\partial x_i} = 0 \tag{2.4.1}$$

describes the conservation of mass in the system, and

$$\frac{\partial \overline{U_i}}{\partial t} + \overline{U_j}\frac{\partial \overline{U_i}}{\partial x_j} = g_i + \frac{1}{\rho}\frac{\partial}{\partial x_j}\left(-\bar{p}\delta_{ij} + \mu\frac{\partial \overline{U_j}}{\partial x_j} - \rho\overline{U_i'U_j'}\right) \tag{2.4.2}$$

describes the conservation of momentum, where

$$-\overline{U_i'U_j'} = \nu_t\frac{\partial \overline{U_i}}{\partial x_j} \tag{2.4.3}$$

is the Reynolds stress term that describes the turbulence. To solve for $-\overline{U_i'U_j'}$ and close the system, we recall that ν_t is the kinematic eddy viscosity, modeled as

$$\nu_t = \frac{a_1 k}{\max\{a_1\omega, \Omega F_2\}} \tag{2.4.4}$$

where k and ω are the kinetic turbulent energy and dissipation of the kinetic energy, respectively. To obtain k and ω, we use the SST $k-\omega$ model, which is given as

$$\frac{D\rho k}{Dt} = \tau_{ij}\frac{\partial \overline{U_i}}{\partial x_j} - \beta^* \rho\omega k + \frac{\partial}{\partial x_j}\left[(\mu + \sigma_k \mu_t)\frac{\partial k}{\partial x_j}\right] \tag{2.4.5}$$

$$\frac{D\rho\omega}{Dt} = \frac{\gamma}{\nu_t}\tau_{ij}\frac{\partial \overline{U_i}}{\partial x_j} - \beta\rho\omega^2 + \frac{\partial}{\partial x_j}\left[(\mu + \sigma_\omega \mu_t)\frac{\partial \omega}{\partial x_j}\right] + 2(\rho - F_1)\rho\sigma_{\omega_2}\frac{1}{\omega}\frac{\partial k}{\partial x_j}\frac{\partial \omega}{\partial x_j} \tag{2.4.6}$$

Using these six coupled equations, (2.4.1)-(2.4.6), we solve for the unknown functions $\mathbf{U}$, p, k, and ω.

3 Methods

The NS boundary conditions, the surface $\partial\Psi$ corresponding to the arterial walls and the initial values for the fields $\mathbf{U}$, p, k, and ω, completely specify a particular solution of the relevant PDEs. Computationally, they specify the initial state of our computational domain Ψ in order for the discretized computation to begin. The solvers within OpenFOAM are programmed to accept a hexahedral mesh, $\delta\Psi$, discretizing the surface $\partial\Psi$ in order to use the finite volume methods. In order to generate the complex boundary

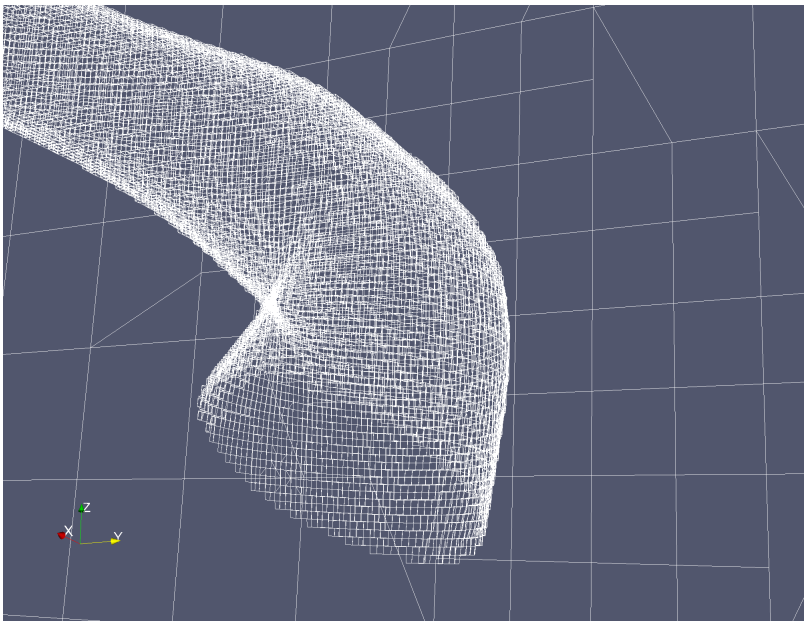

Figure 3: A piece of the discretized surface, our mesh, which we used to specify the boundary conditions to our solver. The render was done during an intermediary step of the construction of the mesh from the STL file created by Blender in order to highlight the cell faces, which become indiscernibly small in the final mesh.

conditions needed to model arterial bifurcations in the Circle of Willis with and without aneurysms, we utilized Blender, an open-source 3-D modeling application, to generate digital models of the geometries we wanted to study. The solids were constructed from tetrahedral faces and exported in triangulated STL (Stereolithography) format. From these, snappyHexMesh, a hexahedral mesh generator contained within OpenFOAM, generated the final mesh that we used to specify the boundary conditions to the solver, as

seen in Figure 3. More specifically, we created a simple bounding box circumscribing our STL solid in order to specify our computational domain to snappyHexMesh. Then, snappyHexMesh took the bounding box and iteratively refined it to snap the computational domain onto the solid, preserving the labels of patches on the bounding box corresponding to inlets and outlets in the arterial structure.

We utilized the PISO (Pressure Implicit with Splitting of Operators) algorithm in the pimpleFoam (PISO - SIMPLE) solver contained within OpenFOAM to generate discrete-time approximations over our entire computational mesh to solutions of the RANS equations with SST $k-\omega$ turbulence. Recall that all solvers in OpenFOAM utilize OpenFOAM's discretization libraries. Also note that the finite volume methods, loosely speaking, involve discretizing the weak form of the NS equations after converting all volume integrals into surface integrals. The fluxes through the discrete cell faces can then be summed to estimate these surface integral terms [24]. At each time step, the implementation of the PISO algorithm in OpenFOAM first solves the discretized momentum equation (with the coupled turbulence terms included) for the pressure. Then the solver enters a loop in which it calculates the flux terms which emerge from the finite volume discretization, corrects for the continuity of the velocity at the outlets, and corrects the whole velocity field based on the new pressure. The final values attained by these last calculations are written out to be used for the next time step, and the whole process begins again. In pimpleFoam, this algorithm is merged with the canonical SIMPLE algorithm by looping through the PISO algorithm, adding relaxation steps after the solution of the momentum equation and before each correction of the velocity. This merging of the PISO and SIMPLE algorithms is called PIMPLE, and is fully delineated in Figure 4.

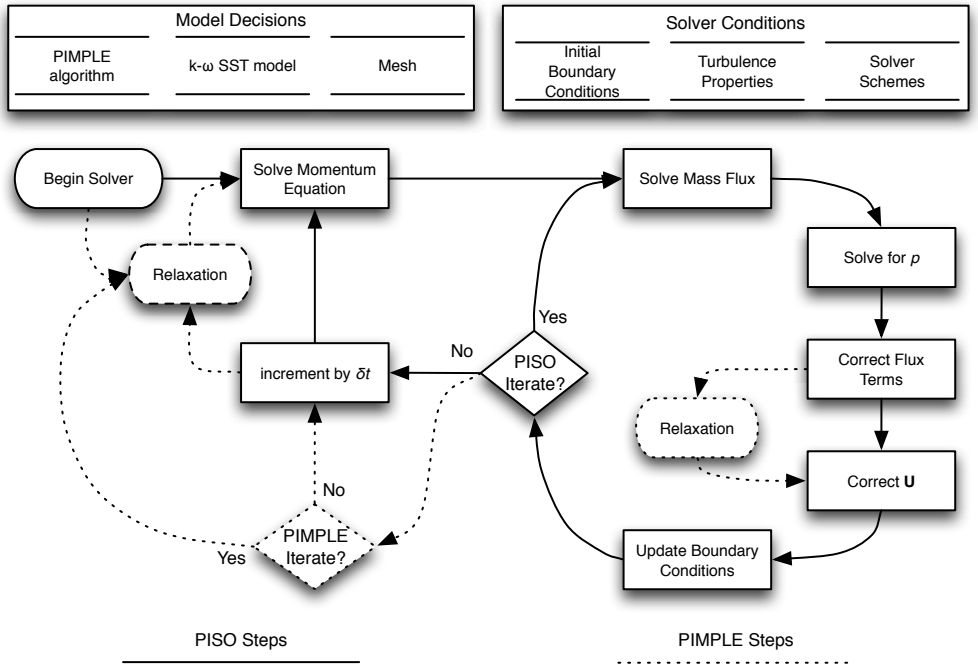

Figure 4: PIMPLE Algorithm Flowchart.

Along the walls, we specify a no-slip boundary condition (see Section 2.1) for velocity and define the normal component (to each cell face) of the gradient of the pressure to be zero (OpenFOAM's 'zeroGradient' patch type). Thus, we have $\nabla p(\mathbf{x}) \cdot \hat{U}_{\delta\Psi i} = 0$, where $\hat{U}_{\delta\Psi i}$ is the unit vector normal to the discretized face $\delta\Psi_i$ centered at $\mathbf{x}$. We define the velocity field at the inlets to agree with clinical measurements of blood flow in the basilar artery and set the inlet pressure to zeroGradient. Outlet velocity is calculated during

the PISO loop when corrections for continuity are made, and we define there to be no inflow back through the outlet, since we are not interested in turbulent conditions near these outlets. Since the Navier-Stokes equations only determine pressure up to a constant, we must define the absolute pressure at some point to determine our solution exactly. We set it to zero on the outlet patch for the initial time step, since we are only concerned with the relative pressure distributions throughout the structure. The parameters involved in the turbulence model, ν_t, k, and ω, are initialized to uniform fields and are allowed to converge to their actual values during the first few time steps.

We recreated the center ring of the Circle of Willis based on fMRI images. We added four saccular aneurysms to the healthy Circle of Willis at sites with high incidence of aneurysm formation (per Figure 1), one per simulation. These aneurysms can be seen in Figure 5 and were designed as nearly spherical protrusions with a diameter of slightly less than 3mm, the point at which clinical consensus mandates surgical intervention [22]. Qualitative measurements were easily accomplished by viewing the results of our simulations with ParaView, a toolkit capable of directly using the data generated by the OpenFOAM solvers. Quantitative analysis was also made possible by ParaView's ability to extract point data from particular regions of the solution space. The relevant measurements were averaged over the apices of the arterial bifurcations to provide an orderable set of data to quantify the increase or decrease in WSS. Additionally, once the aneurysm location that created the largest percentage change in WSS was determined, and said change in WSS found to be negligible, we increased the size of that aneurysm to greater than 3mm in order to exaggerate the downstream effects and further check our results.

4 Results

We verified the integrity of our setup of the pimpleFoam solver using a straight cylinder, a single bifurcation, and a simplified arterial structure consisting of a main bifurcation and two secondary bifurcations. We ran the triple bifurcation model with realistic values for inlet blood velocity over the length of a heartbeat, as shown in Figure 6.

We found that for this simple case, the magnitude of the WSS at the apex of the bifurcations was lower than along the rest of the arterial walls, as expected. As can be seen in Figure 7, the WSS followed the same general distribution regardless of the presence or size of an aneurysm. Predictable variations in pressure were observed over the span of a heartbeat, as seen in Figure 8, including lower pressure along the vessel walls wherever the blood flow was fastest, as well as higher pressure at the apex of the arterial bifurcations where the blood is colliding with the wall directly.

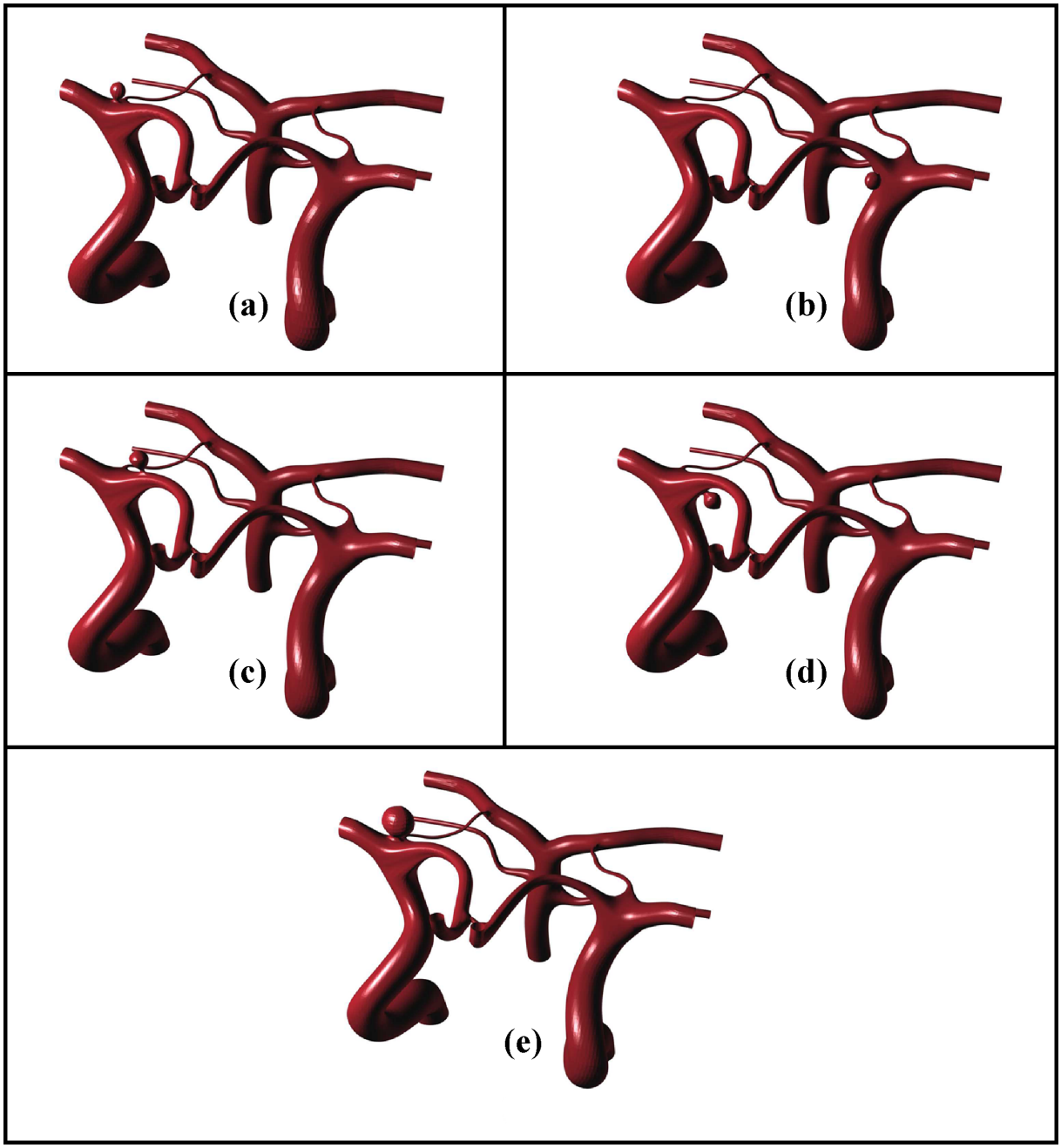

Figure 5: Model Geometries Used. Small aneurysms were placed a) at the junction of the right anterior cerebral artery and the right middle cerebral artery, b) at the junction of the left anterior cerebral artery and the left internal carotid artery, c) on the right anterior cerebral artery, and d) at the junction of the right anterior cerebral artery and the right internal carotid artery. A large aneurysm was placed at the bifurcation of the right anterior cerebral artery and the right middle cerebral artery.

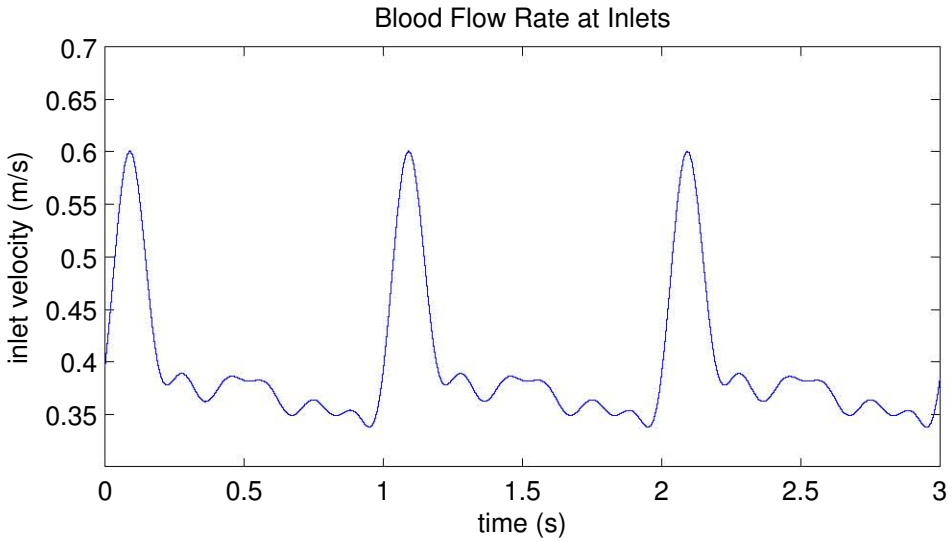

Figure 6: Function used for inlet blood velocity over a heartbeat.

The results obtained from running our simulations through the full Circle of Willis immediately showed that introducing an aneurysm had little if no effect on downstream WSS, as seen in Figures 9 and 10. Locally, notable changes in the velocity fields were observed, as shown by differences in the identically generated streamline seen in Figure 11. However, although the WSS depends on the local velocity fields, no qualitative differences in the WSS distributions were observable there, as also seen in Figure 11, necessitating the extraction of quantitative data.

We extracted sets of points from the values of the WSS fields at the vertices of our discretized cell faces. Our data was takes both from the bifurcation of the right middle cerebral artery and the anterior connecting artery, and from the bifurcation of the right internal carotid artery and the right anterior cerebral artery, as seen in Figure 12, in order to study the magnitude of the WSS with and without an aneurysm present. For each set of points extracted, the magnitude of WSS was averaged across the set in order to analyze its overall change in that region between measurements. Additionally, we averaged data from sets of extracted points from regions on the left and right internal carotid arteries and the left and right anterior cerebral arteries. The averages were utilized to calculate relative percent change.

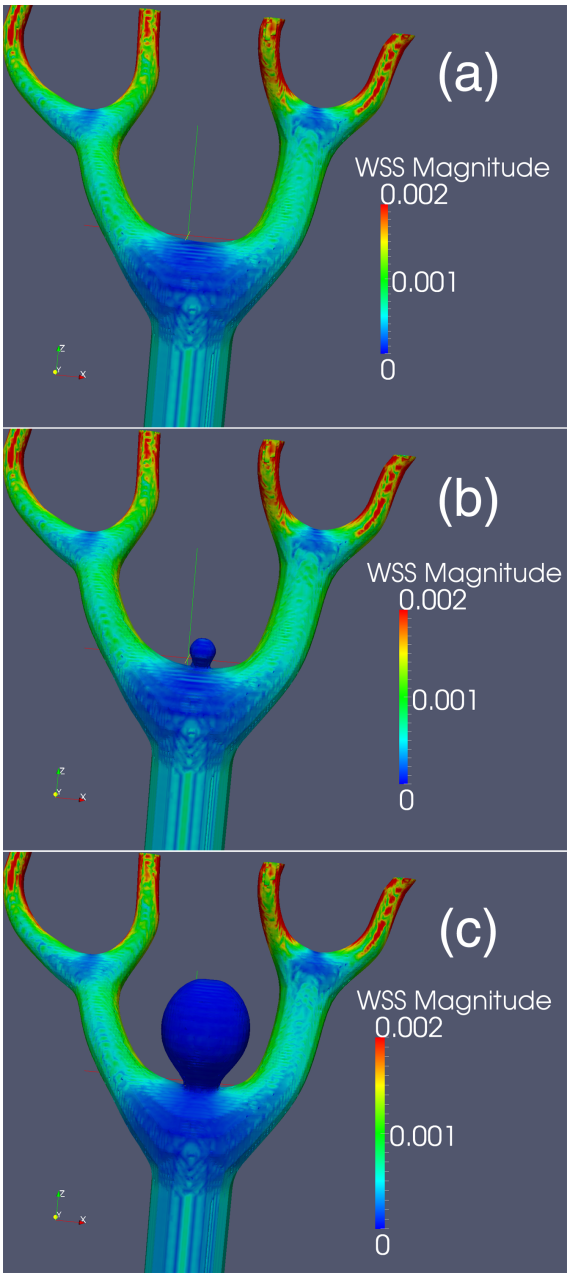

Figure 7: An simplified model. Shown are WSS distributions at peak systole. (a) shows the healthy model, (b) a small aneurysm, and (c) a huge aneurysm. Qualitatively realistic WSS results consistent with [7] and others are observed, including lowered WSS at the apices of bifurcations. However, there is little visible difference in WSS even in the presence of the huge aneurysm.

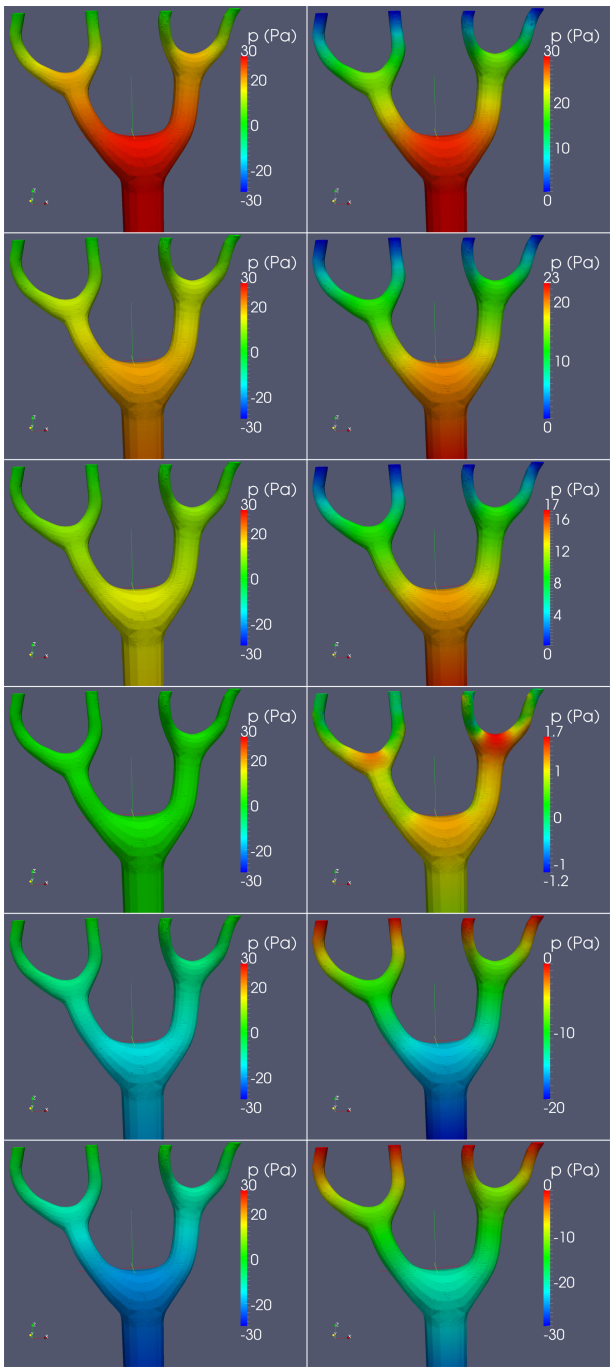

Figure 8: An simplified model of an arterial bifurcation and two bifurcations downstream of it. The left column shows the pressure as it varies from peak systole to peak diastole. Qualitatively realistic results can be seen, including decreased pressure when expected during the cardiac cycle. The right column shows the pressure throughout the model scaled to more precisely evince the distribution of pressure at that particular time step. We see the expected pressure peaks at the arterial bifurcations.

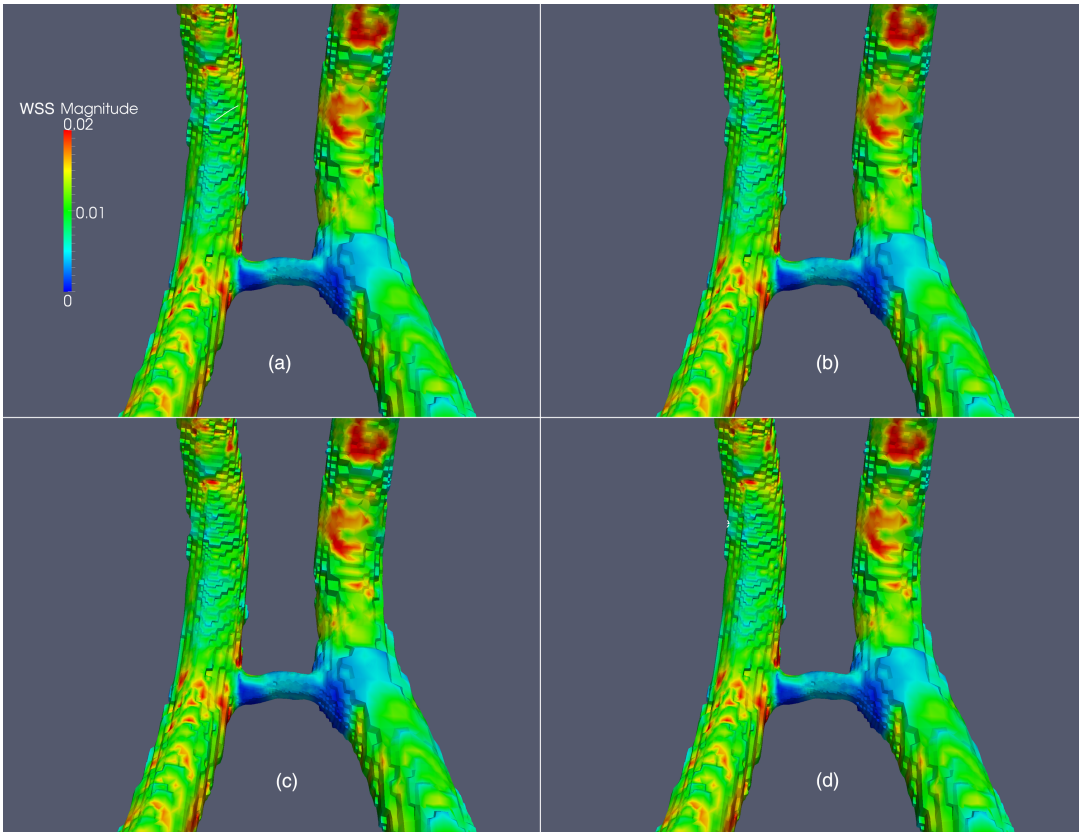

Figure 9: Superior view of the WSS magnitude in the anterior communicating artery region located a) in a healthy Circle of Willis b) downstream of an aneurysm placed at the junction of the right anterior cerebral artery and the right middle cerebral artery c) downstream of an aneurysm placed at the junction of the left anterior cerebral artery and the left middle cerebral artery d) downstream of an aneurysm placed on the right anterior cerebral artery. The lack of change in the presence of an aneurysm is obvious.

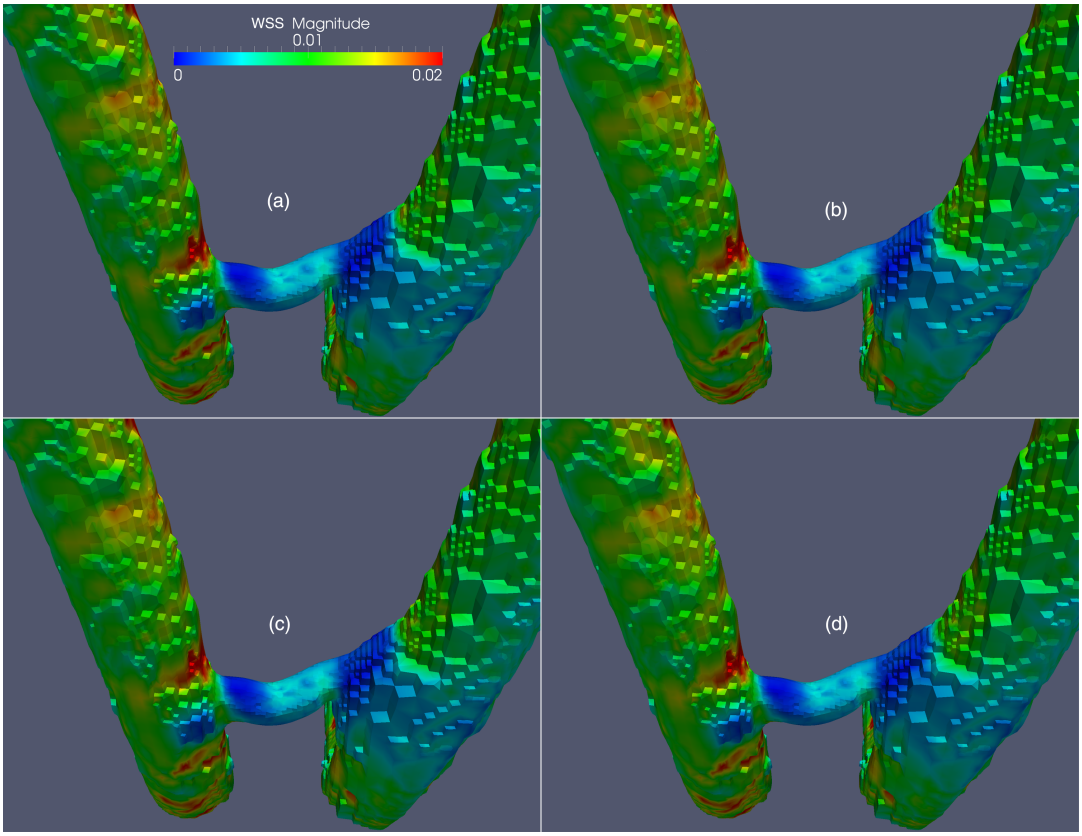

Figure 10: Inferior view of the results presented in Figure 9. Again notice the lack of change upon introduction of an aneurysm.

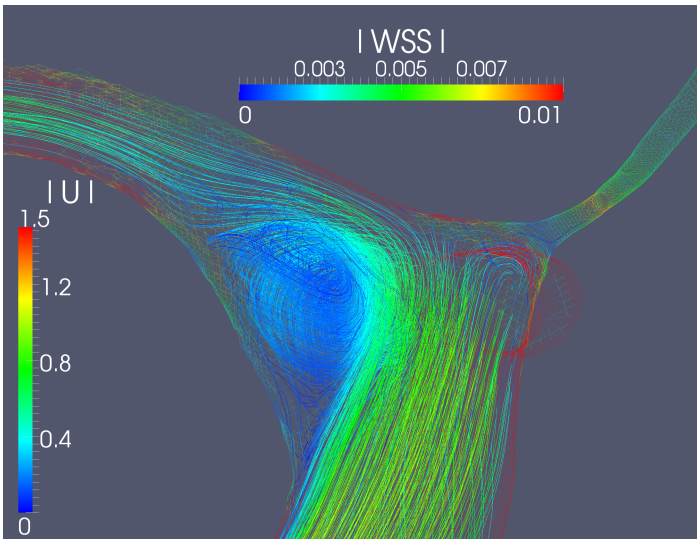

(a)

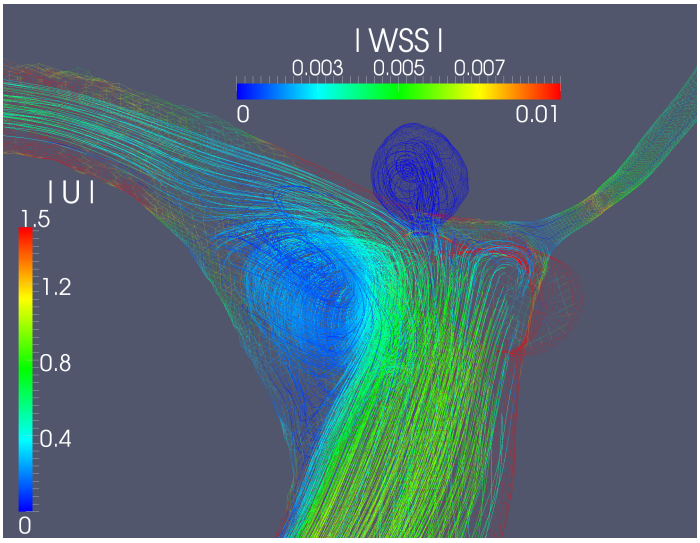

(b)

Figure 11: Turbulent dynamics at the right internal carotid artery bifurcation with (a) and without (b) an aneurysm. Walls are colored by the magnitude of the WSS at that point, and the streamlines, found using a standard Runga-Kutta 4-5 type integrator, are colored by the magnitude of the velocity. We see that for the identically generated streamlines there are visible, though mild, changes in the streams produced, suggesting that an aneurysm does have an appreciable effect on the flow of blood in its vicinity. However, we see, as in the simplified model in Figure 7, no appreciable change in the WSS near the aneurysm.

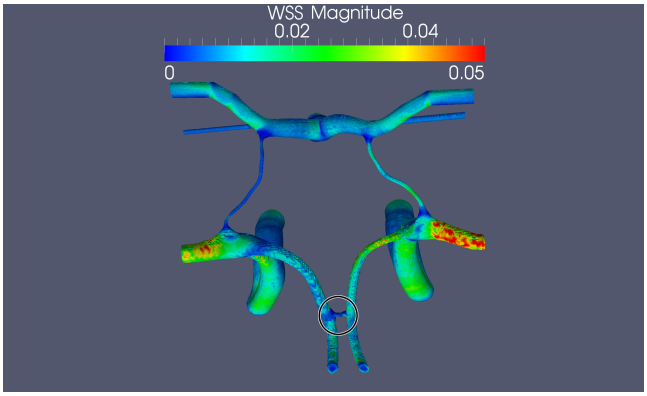

(a)

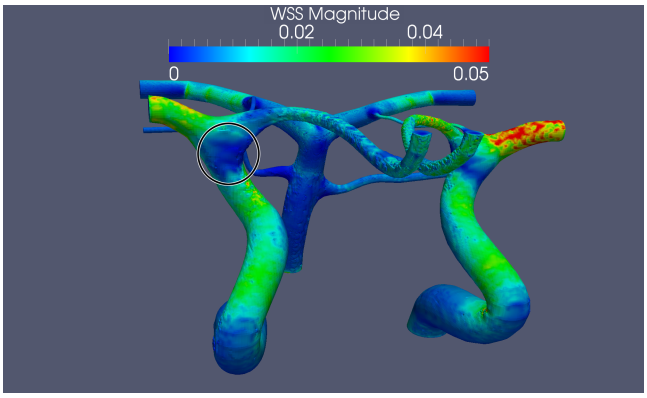

(b)

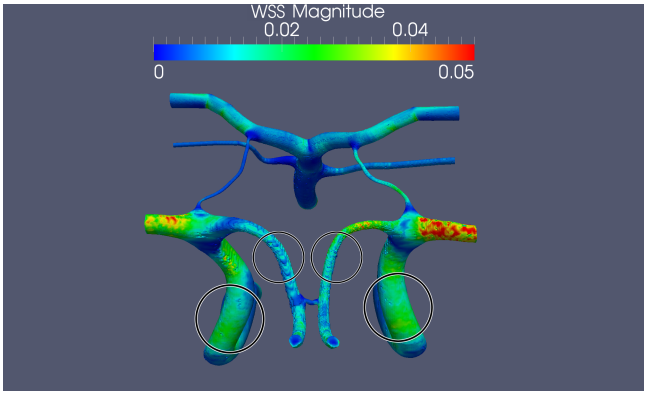

(c)

Figure 12: Locations of extracted data points. a) Bifurcation of the right middle cerebral artery and the anterior connecting artery b) Bifurcation of the right internal carotid artery and the right anterior cerebral artery c) Left and right internal carotid arteries and the left and right anterior cerebral arteries.

We find the expected drops in WSS generally attributed to primary aneurysm formation in the Circle of Willis, that is, the change between stresses on the walls of the arteries and the stresses on the healthy arterial bifurcation. These are found to be approximately 90% between a healthy right anterior cerebral artery and a healthy right internal carotid artery bifurcation and on the order of 70% between a healthy right anterior cerebral artery and a healthy right anterior connecting artery bifurcation. Introducing an aneurysm in various common orientations on the internal carotid artery bifurcations causes a further decrease in WSS, both locally to the aneurysm and downstream at the anterior connecting artery, even though these were not apparent from the graphics. The changes, however, are only on the order of a 0-4% decrease from the healthy levels of WSS at said bifurcations. Further, if we measure the difference between a healthy arterial wall and a healthy bifurcation, call it the healthy difference, and the difference between a healthy arterial wall and a diseased bifurcation, call it the diseased difference, we see that the diseased difference is less than 1% larger than the healthy difference for all data generated. These measurements can be seen summarized in Table 4.

Measure	Healthy	Aneurysm 1	Aneurysm 2	Aneurysm 3	Aneurysm 4	Aneurysm 5
RICAB Value	0.001953	0.001906	0.001939	0.001952	0.001945	0.001861
H (%)	0.00	-2.41	-0.73	-0.06	-0.416013	-4.71
RICA (%)	-90.59	-90.81	-90.66	-90.59	-90.63	-91.03
LICA (%)	-88.73	-88.10	-88.80	-88.73	-88.77	-89.26
RACAB Value	0.003110	0.003052	0.003011	0.003046	0.003060	0.002988
H (%)	0.00	-1.87	-3.19	-2.05	-1.59	-3.90
RACA (%)	-71.27	-71.80	-72.18	-71.85	-71.72	-72.39
LACA (%)	-83.70	-84.00	-84.22	-84.03	-83.96	-84.33

Table 4: Values for average magnitude of WSS for the right internal carotid artery bifurcation (RICAB) and the right anterior connecting artery bifurcation (RACAB). Percentage change computed compared to the same location on the healthy geometry (H) and compared to values upstream on the right/left internal carotid artery (R/LICA)and right/left anterior cerebral artery (R/LACA) respectively. That is, (Aneurysm-Healthy)/Healthy. Aneurysms are numbered as shown in Figure 5.

5 Discussion

It is clear that with a percent change of between 0-4%, the WSS on the right anterior communicating artery bifurcation and the right internal carotid artery bifurcation is nearly unaffected by the presence of an aneurism at the bifurcations around the internal carotid artery. More specifically, since the relative percent decrease in WSS near areas with a high incidence of aneurysm formation compared to the upstream arterial wall is between 70% and 91%, we suggest that a relative decrease of 4% at a typically low WSS locus is insignificant, especially since the incidence of aneurysm formation at that locus is already so large. This result is an indication that individuals with multiple aneurysms develop the secondary aneurysms not due to an upstream aneurysm but because of other factors.

We found that the WSS immediately surrounding the aneurysm differed similarly to the stresses on downstream regions. The presence of an aneurysm again decreased the average value of WSS by an insignificant percentage when compared to the changes in stresses between the areas of low and high incidence of aneurysm formation along the vessel walls. This suggests that, even locally, the presence of a primary aneurysm is not likely to instigate the formation of a second. Instead, whatever forces instigate the first aneurysm are likely to be almost exclusively the culprits of the secondary aneurysm's formation.

6 Conclusion

We utilized the NS equations to study the effects of a primary aneurysm on downstream arterial bifurcations located in the Circle of Willis. To numerically solve these equations, we ran simulations through 3-D models of the Circle of Willis in OpenFOAM using the equations for incompressible turbulent fluid flow as modeled by the SST $k - \omega$ model. We used OpenFOAM's built in tools to obtain WSS magnitudes at every point defining the boundary of the Circle of Willis.

We measured the relative effect of an intracranial aneurysm on the WSS on downstream arterial walls and found a seemingly negligible 0-4% relative decrease, regardless of the size and location of the primary aneurysm. This result suggests that a primary aneurysm has little effect on the formation of secondary aneurysms; the occurrences of multiple intracranial aneurysms appear to be independent events. Thus, we suggest that the state of the arterial walls must be the primary agent in secondary aneurysm formation.

7 Future Work

We would like to see an extension of our model introduce variable flow to mimic the oscillations of pressure and velocity due to heart beats. This extension is already coded and working; it would simply require a larger allocation of computing power to run over a reasonable time length.

Although our results suggest that variations in hemodynamics within the Circle of Willis due to aneurysm formation have a negligible effect on stresses on the arterial walls, they do not guarantee that aneurysms form independently of one another, that is, solely due to pre-existing or induced weakness in the arterial walls. Further work to verify the independence of aneurysm formation would have to take into account dynamic or immersed boundary conditions to reproduce clinical incidence rates of secondary aneurysm formation given realistic decreases in wall integrity.

Finally, we focused on a pair of arterial bifurcations that have some of the highest aneurysm incidence rate and neglected others of marginally less significance, which could possibly display vastly different results. Specifically, the multiple arterial bifurcations on the middle cerebral arteries are more densely clustered and may generate promising results.

Acknowledgments
We would like to thank Dr. Carlos Castillo-Chavez, Executive Director of the Mathematical and Theoretical Biology Institute (MTBI), for giving us the opportunity to participate in this research program. We would also like to thank Co-Executive Summer Directors Dr. Erika T. Camacho and Dr. Stephen Wirkus for their efforts in planning and executing the day to day activities of MTBI. We would like to dedicate this paper in loving memory of Dr. Mario Beltran, M.D. We also want to give special thanks to Dr. Sumni Lee and Jonathan Burkow. This research was conducted in MTBI at the Mathematical, Computational and Modeling Sciences Center (MCMSC) at Arizona State University (ASU). This project has been partially supported by grants from the National Science Foundation (NSF - Grant DMPS-0838705), the National Security Agency (NSA - Grant H98230-11-1-0211), the Office of the President of ASU, and the Office of the Provost of ASU.

References

[1] M. S. Alnaes, J. Isaksen, K. A. Mardal, B. Romner, M. K. Morgan, and T. Ingebrigtsen. Computation of hemodynamics in the circle of Willis. *Stroke*, 38(9):2500–2505, Sep 2007.

[2] J. Banks and N. W. Bressloff. Turbulence Modeling in Three-Dimensional Stenosed Arterial Bifurcations. *Journal of Biomechanical Engineering*, 129:40–51, Feb 2007.

[3] R. Berguer, J. L. Bull, and K. Khanafer. Refinements in mathematical models to predict aneurysm growth and rupture. *Ann. N. Y. Acad. Sci.*, 1085:110–116, Nov 2006.

[4] L. Davidson. Turbulence modelling. http://www.tfd.chalmers.se/ lada/postscript_files/solids-and-fluids_turbulent-flow_turbulence-modelling.pdf, July 2006.

[5] L. Davidson. *An Introduction to Turbulence Models*. Chalmers Publishing Company, New York, 2011.

[6] L. Davidson. Fluid mechanics, turbulent flow and turbulence modeling. lada@chalmers.se, July 2012.

[7] P. Di Achille and J. D. Humphrey. Toward large-scale computational fluid-solid-growth models of intracranial aneurysms. *Yale Journal of Biology and Medicine*, 2(85):pp. 217–228, 2012.

[8] H. Eldawoody, H. Shimizu, N. Kimura, A. Saito, T. Nakayama, A. Takahashi, and T. Tominaga. Simplified experimental cerebral aneurysm model in rats: Comprehensive evaluation of induced aneurysms and arterial changes in the circle of willis. *Brain Research*, 1300(0):159 – 168, 2009.

[9] N. Hashimoto and F. Hazama. Experimentally induced cerebral aneurysms as model for non-surgical treatment. *Journal of Clinical Neuroscience*, 1(4):266 – 273, 1994.

[10] H. Jasak. *Error Analysis and Estimation for the Finite Volume Method with Applications to Fluid Flows*. PhD thesis, University of London, 1996.

[11] S. Juvela. Risk factors for multiple intracranial aneurysms. *Stroke*, 31(2):392–397, Feb 2000.

[12] Y. Kim, S. Lim, S.V. Raman, O.P. Simonetti, and A. Friedman. Blood flow in a compliant vessel by the immersed boundary method. *Annals of Biomedical Engineering*, 37(5):927–942, May 2009.

[13] X. Lv, Z. Wu, Y. Li, C. Jiang, X. Yang, and J. Zhang. Cerebral arteriovenous malformations associated with flow-related and circle of willis aneurysms. *World Neurosurgery*, 76(5):455 – 458, 2011.

[14] J. M. McDonough. Introductory lectures on turbulence. www.engr.uky.edu/ acfd/lctr-notes634.pdf, 2011.

[15] F. R. Menter. Two-Equation Eddy-Viscosity Turbulence Models for Engineering Applications. *AIAA Journal*, 32(8):1598–1605, August 1994.

[16] A. M. Nixon. The critical role of hemodynamics in the development of cerebral vascular disease a review. *Journal of neurosurgery*, 112, 2010.

[17] S. Peng, P. Eliasson, and L. Davidson. Examination of the shear stress transport assumption with a low-reynolds number k-ρ model. *AIAA Journal*, 2007.

[18] A. I. Qureshi, J. I. Suarez, P. D. Parekh, G. Sung, R. Geocadin, A. Bhardwaj, R. J. Tamargo, and J. A. Ulatowski. Risk factors for multiple intracranial aneurysms. *Neurosurgery*, 43(1):22–26, Jul 1998.

[19] D. M. Sforza, R. Lohner, C. Putman, and J. Cebral. Hemodynamic Analysis of Intracranial Aneurysms with Moving Parent Arteries: Basilar Tip Aneurysms. *Int j numer method biomed eng*, 26(10):1219–1227, Oct 2010.

[20] D. M. Sforza, C. M. Putman, and J. R. Cebral. Hemodynamics of Cerebral Aneurysms. *Annu Rev Fluid Mech*, 41:91–107, Jan 2009.

[21] W.E. Stehbens and D. Phil. Etiology of intracranial berry aneurysms. *Journal of Neurosurgery*, 70(6):823–831, June 1989.

[22] C. Vega, J. V. Kwoon, and S. D. Lavine. Intracranial aneurysms: current evidence and clinical practice. *Am Fam Physician*, 66(4):601–608, Aug 2002.

[23] S. M. Wasserman and J. N. Topper. Adaptation of the endothelium to fluid flow: in vitro analyses of gene expression and in vivo implications. *Vasc Med*, 9(1):35–45, Feb 2004.

[24] G.X. Wu and Z.Z. Hu. A taylor series-based finite volume method for the navier-stokes equations. *International Journal for Numerical Methods in Fluids*, Apr 2008.

[25] N. Zaorsky. The most common sites of intracranial saccular aneurysms. http://en.wikipedia.org/wiki/File:Wikipedia_intracranial_aneurysms_-_inferior_view_-_heat_map.jpg, January 2011.